

Research Article

Damage Deformation of Flexure-Yielding Steel-Reinforced Concrete Coupling Beams: Experimental and Numerical Investigation

Yinghui Li,^{1,2} Huanjun Jiang ^{1,2} and T. Y. Yang^{2,3}

¹State Key Laboratory of Disaster Reduction in Civil Engineering, Tongji University, Shanghai, China

²The International Joint Research Laboratory of Earthquake Engineering, Tongji University, Shanghai, China

³Department of Civil Engineering, University of British Columbia, Vancouver, Canada

Correspondence should be addressed to Huanjun Jiang; jhj73@tongji.edu.cn

Received 20 February 2019; Revised 8 May 2019; Accepted 27 May 2019; Published 13 June 2019

Academic Editor: Zhongguo John Ma

Copyright © 2019 Yinghui Li et al. This is an open access article distributed under the Creative Commons Attribution License, which permits unrestricted use, distribution, and reproduction in any medium, provided the original work is properly cited.

SRC coupling beams offer many significant advantages, including the reduction in section depth, reduced congestion at the wall boundary region, improved degree of coupling for a given beam depth, and improved deformation capacity. In this paper, 7 half-scale flexure-yielding SRC coupling beams designed according to Chinese approach have been tested under cyclic loads. Detailed parameters such as aspect ratios, steel reinforcement ratios, and steel flange-web ratios were systematically studied, and the damage behavior of SRC coupling beams were presented in this paper. The test results show that the aspect ratio, steel ratio, and steel flange-web ratio have great influence on the damage behavior of SRC coupling beams. Three-dimensional nonlinear finite element models were constructed and benchmarked through comparison with test results for both global and local damage deformation behavior. Based on the material damage and strength degradation, four performance levels were defined and corresponding chord rotation limits were obtained through the verified numerical analysis.

1. Introduction

Reinforced concrete shear wall (RCSW) with the coupling beam is one of the most prevalent seismic force resisting systems used for medium- and high-rise constructions worldwide [1]. In this structural system, seismic forces are resisted through a combination of flexural action of the shear walls and frame action between the shear walls and coupling beams. Under such frame action, the coupling beams should be properly designed to transfer adequate forces between adjacent walls. In addition, coupling beams are expected to be used as primary fuses to dissipate earthquake energy as they undergo inelastic deformation [2]. Therefore, the deformation capacity and energy dissipation capacity are also important for coupling beams.

Conventionally reinforced concrete coupling beam design typically results in diagonally reinforced deep beam to satisfy the stiffness, strength, and energy dissipation demands while creates constructability challenges and

increases construction time and cost. Steel-reinforced concrete (SRC) coupling beams provide an attractive alternative, thanks to its more attractive behavior. SRC coupling beams offer potential advantages of reduced section depth, reduced congestion at the wall boundary region, improved degree of coupling for a given beam depth, and improved deformation capacity [3]. Therefore, reinforced concrete shear wall (RCSW) with steel-reinforced concrete (SRC) coupling beams is one of the new innovations in the composite seismic force resisting systems and has been widely used in Asia and North America.

Gong and Shahrooz [4] tested four one-third-scale shear-yielding SRC coupling beams and found that reinforced encasement around the steel enhanced the strength and stiffness. Based on an equation developed and calibrated to test results by Gong and Shahrooz [5], the 2010 AISC Seismic Provisions [Eq. (H5-3)] recommend computing the expected shear strength, V_{ne} , of an SRC coupling beam as

$$V_{ne} = 1.1R_y(0.6f_a t_w (H_s - 2t_f)) + 1.56 \left(0.17 \sqrt{f_c} b h_0 + \frac{A_{st} f_{yt} h_0}{s} \right), \quad (1)$$

where f_c is the nominal compressive strength of the concrete, b_c is the beam section width, h_0 is the beam section effective depth, A_{st} is the area of transverse reinforcement, f_{yt} is the nominal yield strength of transverse reinforcement, s is the spacing of transverse reinforcement, R_y is the ratio of the expected to nominal yield strength of structural steel, f_a is the nominal yield strength of structural steel, t_w is the web thickness of encased steel, H_s is the cross-sectional height of encased steel, and t_f is the flange thickness of encased steel. Su and Lam [6] tested eight half-scale steel plate-reinforced concrete coupling beams of short and medium-length spans and proposed a unified design approach. Motter et al. [3] tested four one-half scale flexure-yielding SRC coupling beams embedded into reinforced concrete structural walls for realistic loading conditions and found that with adequate encased steel embedment and wall reinforcement, the performance of flexure-yielding SRC coupling beams can meet or exceed that of conventionally or diagonally reinforced concrete coupling beams. Motter et al. [7] modified equation (1) to calculate nominal shear strength of SRC coupling beams as follows:

$$V_n = 0.6f_a t_w (H_s - 2t_f) + 0.17 \sqrt{f_c} b h_0 + \frac{A_{st} f_{yt} h_0}{s}. \quad (2)$$

Although a number of SRC coupling beams have been tested [4–8], those results generally showed that SRC coupling beams can provide good seismic behavior; stirrups, longitudinal rebars, and embedment of encased steel have a significant impact on the failure modes of SRC coupling beams. However, those researches paid little attention to SRC coupling beam damage development during the whole loading process, which is an important reference in assessing the seismic performance of structures or structural components [9, 10]. In addition, there are two main types of encased steel used in composite coupling beams, which are H-shaped steel [3–5, 7, 8] and steel plate without flange [6]. However, the comparison research between these two types of encased steel on seismic performance of coupling beams is limited.

In this paper, the cyclic test of 7 half-scale flexure-yielding SRC coupling beams designed according to Chinese code JGJ138-2016 [11] is presented and damage development was recorded throughout the whole loading process. The main design parameters studied are aspect ratio (span-to-depth ratio), steel ratio (ratio of encased steel section area to beam section area), and steel flange-web ratio (ratio of flange steel section area to web steel section area of encased steel). In order to develop further insight into the observed experimental behavior, this paper also presents the development and benchmarking of detailed 3D nonlinear finite element models for predicting the damage behavior of the tested SRC coupling beams. The models explicitly account for material inelasticity including concrete cracking

and interaction behavior between rebar, encased steel, and concrete and are benchmarked using results from the experimental program. Based on the damage characters and strength degradation, four performance levels were defined and corresponding chord rotation limits were obtained through the verified numerical analysis.

2. Test Program

2.1. Test Specimens. Seven half-scale SRC coupling beams with various span lengths and steel configurations were tested. To ensure the SRC coupling beams are well connected to the concrete pedestal, an embedment length of encased steel welded with shear studs and longitudinal bars in the pedestal is selected as 700 mm, which is more than sufficient to be treated as a fixed boundary condition. The calculation for the embedment length of encased steel will be discussed at the end of this section. Since this study just focuses on the damage deformation of SRC coupling beams, the damage deformation of wall piers that are connected to SRC coupling beams is expected to be zero. Therefore, the pedestal is constructed not to simulate a shear wall but just to serve as a rigid block to fix the SRC coupling beams, and the rebar in pedestal is designed more than enough to resist shear and moment from the coupling beam end. In addition, as the SRC coupling beams are designed as flexure-yielding which behavior is expected to be governed by flexure, only half of the SRC coupling beam instead of the whole span is tested in the laboratory, which is similar to other researches [3–5,7]. The beam specimens are free to elongate in this test since the axial load from restrained adjacent coupled walls is approximately 4–7% of axial load capacity of coupling beams [12], which is relatively small and is negligible in this research. To ensure the bonding between the encased steel and concrete, 10 mm diameter shear studs spaced at a distance of 100 mm were welded on the flange and web of encased steel according to Chinese code JGJ138-2016 [11].

The cross sections of specimens are identical that the height is 500 mm and width is 300 mm, and the longitudinal and transverse reinforcements of specimens are also identical. Figure 1 shows the dimensions of the specimens, the steel reinforcement and encased steel details, and the perspective view of the specimens. The detailed design parameters especially the beam length and encased steel configuration of specimens are shown in Table 1. Specimens Beam1, Beam2, and Beam3 have all the parameters same except the aspect ratio (span-to-depth ratio is equal to $2L/500$). Specimens Beam1, Beam4, and Beam5 have all the parameters same except the steel flange-web ratio (area ratio of flange steel to web steel of encased steel is equal to $2t_f B_s / (H_s - 2t_f) / t_w$). Specimens Beam2, Beam6, and Beam7 have all the parameters same except the steel ratio (steel ratio is equal to $(H_s t_w + 2(B_s - t_w)t_f) / 150000$). The tensile test results of the steel plate and steel bar are listed in Table 2. The concrete cubic compressive strength f_{cu} is 57.8 MPa.

The flexural capacity and shear capacity of specimens were calculated based on the tested material strength, and the corresponding resistance capacity of specimens is shown in Table 3. The flexural capacity was calculated using

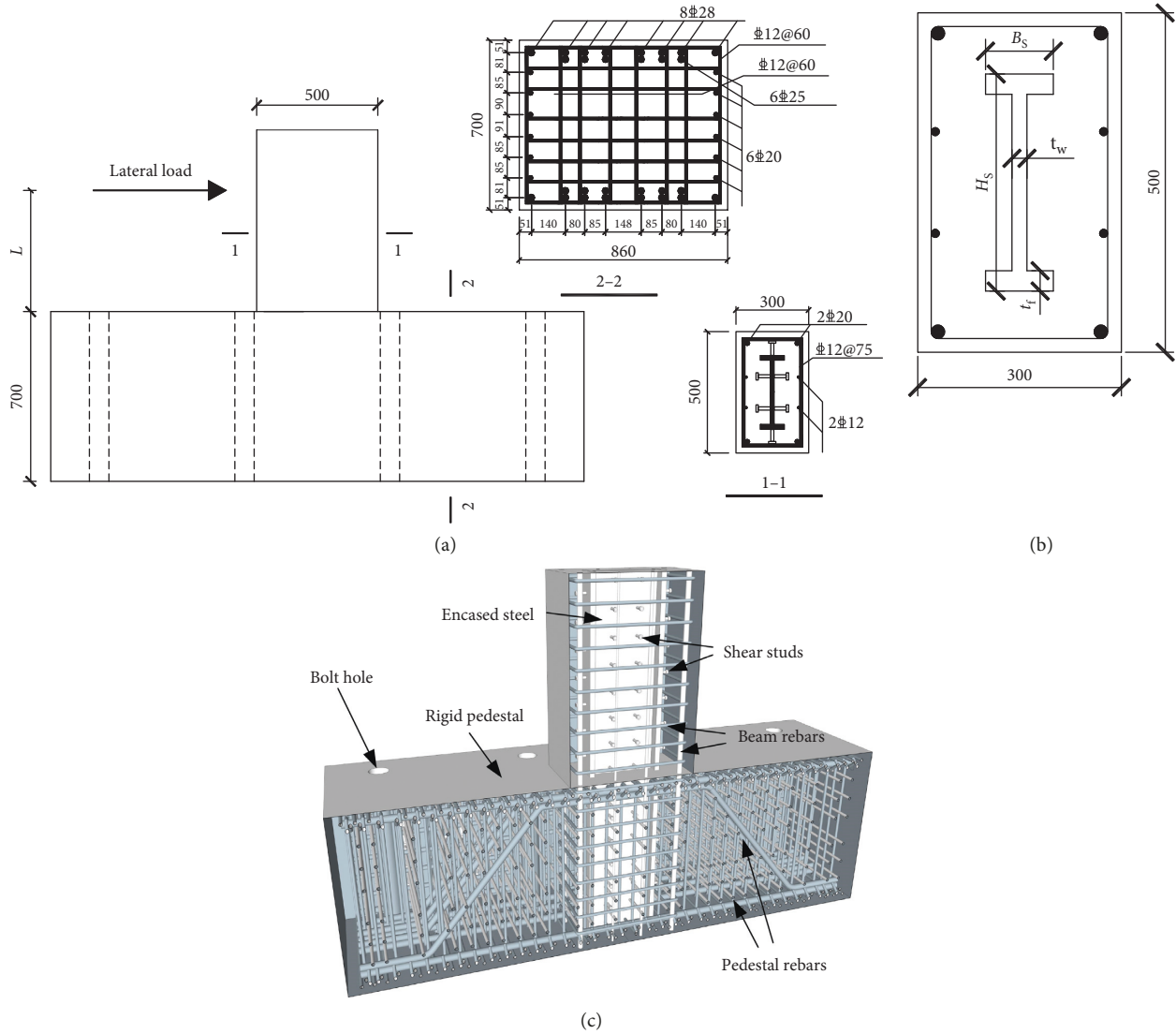


FIGURE 1: (a) Dimensions of the specimens and the steel reinforcement details (unit: mm). (b) Encased steel details (unit: mm). (c) Perspective view of the specimens.

TABLE 1: Detailed parameters of specimens.

Specimen number	Loading point distance L (mm)	Cross-sectional dimensions of encased steel (mm)				Steel ratio (%)	Aspect ratio	Steel flange-web ratio
		H_s	B_s	t_w	t_f			
Beam1	500	290	90	16	20	5.0	2	0.92
Beam2	750	290	90	16	20	5.0	3	0.92
Beam3	1250	290	90	16	20	5.0	5	0.92
Beam4	500	292	80	20	16	5.0	2	0.46
Beam5	500	300	—	25	—	5.0	2	0
Beam6	750	300	120	20	20	6.7	3	0.92
Beam7	750	310	120	25	25	8.3	3	0.92

Notes: H_s represents the cross sectional height; B_s represents the flange width; t_w represents the web thickness; t_f represents the flange thickness.

equations in Chinese code JGJ138-2016 [11] and fiber section analysis, respectively. The shear capacity was calculated by using equations in Chinese code JGJ138-2016 and

equation (2) proposed by Motter et al. [7], respectively. The flexural capacity and shear capacity equations of SRC coupling beam with a symmetrical rebar and symmetrical

TABLE 2: Tensile test results of the encased steel plate and steel bar.

Dimension of the steel plate or bar	Yielding strength (MPa)	Tensile strength (MPa)	Elastic modulus (MPa)	Yielding strain	Tensile strain
Plate thickness of 16 mm	249.1	411.2	1.95×10^5	1.28×10^{-3}	0.214
Plate thickness of 20 mm	282.0	452.9	2.06×10^5	1.37×10^{-3}	0.206
Plate thickness of 25 mm	255.0	409.5	2.06×10^5	1.24×10^{-3}	0.215
Rebar diameter of 12 mm	457.0	555.6	1.90×10^5	2.41×10^{-3}	0.139
Rebar diameter of 20 mm	437.5	582.8	1.96×10^5	2.23×10^{-3}	0.133

TABLE 3: Lateral load resistance capacity of specimens (kN).

Specimen number	Calculated by M_n/L		Calculated by V_n	
	Fiber section	Equation (3)	Equation (2)	Equation (4)
Beam1	951.4	919.8	1189.1	1116.2
Beam2	634.3	613.2	1189.1	1200.0
Beam3	380.6	367.9	1189.1	1200.0
Beam4	963.6	927.7	1390.0	1309.4
Beam5	904.4	879.7	1535.4	1449.2
Beam6	773.9	761.1	1431.2	1404.3
Beam7	841.5	829.6	1546.3	1516.1

encased steel in Chinese code JGJ138-2016 are shown as follows:

$$M_n = \alpha_1 f_c b x \left(h_0 - \frac{x}{2} \right) + f_y A_s (h_0 - a'_s) + f_a A_{af} (h_0 - a'_a) + M_{aw}, \quad (3a)$$

$$\alpha_1 f_c b x + \left[2.5 \frac{x}{h_0} - (\delta_1 + \delta_2) \right] t_w h_0 f_a = 0, \quad (3b)$$

$$M_{aw} = \left[0.5(\delta_1^2 + \delta_2^2) - (\delta_1 + \delta_2) + 2.5 \frac{x}{h_0} - \left(1.25 \frac{x}{h_0} \right)^2 \right] t_w h_0^2 f_a, \quad (3c)$$

$$V_n = \begin{cases} 0.38 f_t b h_0 + 0.9 \frac{A_{st} f_{yt} h_0}{s}, & \text{aspect ratio} \leq 2.5, \\ 0.42 f_t b h_0 + \frac{A_{st} f_{yt} h_0}{s}, & \text{aspect ratio} > 2.5, \end{cases} \quad (4)$$

where α_1 is the coefficient modifying the compression stress of concrete compression zone, x is the effective depth of concrete compression zone, f_y is the nominal yield strength of longitudinal reinforcement, A_s is the area of longitudinal reinforcement, a'_s is the distance from center of compression rebar to the edge of compression zone, A_{af} is the area of encased steel flange, a'_a is the distance from center of compression encased steel flange to the edge of compression zone, $\delta_1 h_0$ is the distance from upper edge of encased steel web to the edge of compression zone, $\delta_2 h_0$ is the distance from lower edge of encased steel web to the edge of compression zone, and f_t is the nominal tensile strength of the concrete. A similar result for moment capacity and shear capacity was obtained using different equations or methods, which proves the accuracy of the

equations or methods. In addition, the lateral load resistance capacity calculated by M_n/L is smaller than that calculated by V_n , which testifies the flexure-yielding design intention.

The minimum required embedment length of encased steel L_e is determined using Equation H4-2 in the 2010 AISC Seismic Provisions by taking $V_{n,embed}$ equal to M_n/L , which equation is modified considering the effect of concrete cover [3] and is shown as follows:

$$V_{n,embed} = 4.05 \sqrt{f_c} \left(\frac{t_{wall}}{B_s} \right)^{0.66} \beta_1 B_s (L_e - c) \cdot \left(\frac{0.58 - 0.22 \beta_1}{0.88 + ((L + c)/(L_e - c))} \right), \quad (5)$$

where $V_{n,embed}$ is the shear capacity of the embedded steel, t_{wall} is the thickness of the shear wall connected to SRC coupling beams and is taken as 860 mm in this study which is the width of the pedestal, β_1 is the depth factor, relating the depth of the Whitney stress block to the neutral axis depth, and c is the concrete cover thickness of the pedestal. The maximum required embedment length of seven SRC coupling beam specimens calculated using equation (5) is 435 mm. Considering the connection between lateral hydraulic actuator and reaction wall in the laboratory, the embedment length (the height of the pedestal) is determined to be 700 mm, which is more than sufficient to fix the SRC coupling beam specimens.

2.2. Test Setup. The test setup that is illustrated in Figure 2 was used in this study, which consists of a rigid floor, a reaction wall, a hydraulic actuator, instrumentations, and data acquisition systems. The specimens were tested under reversed cyclic lateral load using the servo-controlled hydraulic actuator. Before the specimen reaching the yielding

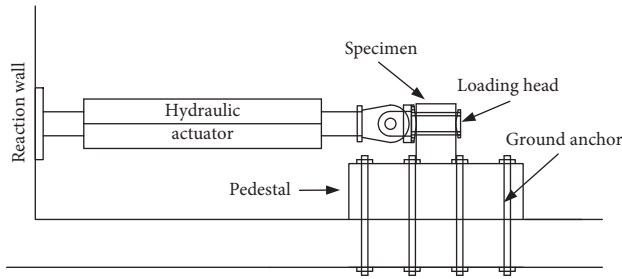


FIGURE 2: Schematic representation of test setup.

point which was monitored by the outmost strain gauges attached to the encased steel, the lateral load was controlled by force and just one reversed cycle was loaded during each loading level. Then after that, the lateral load was controlled by displacement and three reversed cycles were loaded during each loading level. The lateral loading protocol of specimen Beam1 is shown in Figure 3, and each reversed loading cycle was finished in 2 minutes.

Linear variable displacement transducers (LVDTs) were installed to the specimens to measure the lateral displacements and the curvatures in the critical regions. Strain gauges were attached to measure the strain of steel plates and steel bars at plastic hinge zones. The values of the lateral load, the global and local displacements, and the strains were recorded automatically through the data acquisition system throughout the whole loading process. Typical damage states including crack evolution, concrete crushing and spalling, and rebar buckling and fracture were recorded through observation and photographs during the loading process. During the first cycle of each loading level, the maximum crack width was measured at largest lateral load or largest displacement and the corresponding maximum residual crack width was measured at zero loads. The crack width was measured using the crack comparison card, which has a measurement range of 0.02–5 mm.

3. Test Results

3.1. Damage Behavior. The sequence of observed typical damage states is similar for all specimens, and the typical damage states of specimen Beam1 at different loading levels are illustrated in Figure 4, which is a representative for all specimens. In general, the damage started by forming horizontal cracks at the bottom of the specimen at the tension side, as shown in Figure 4(a). Then, the oblique cracks started to appear when the lateral load reaches 500 kN, as shown in Figure 4(b). Tensile yielding of the steel flange was detected using strain gauges with the increase of loading levels. At this instant, the force control loading protocol was switched to the displacement control mode. Afterwards, the initial concrete crushing of compressive side at the bottom of the specimen was observed when lateral displacement reaches 10 mm, as shown in Figure 4(c). Under the following load cycles, the large cracks concentrated at the interface, as shown in Figure 4(d). Then, the spalling of concrete cover appeared when the lateral displacement

reaches 22.5 mm, as shown in Figure 4(e). At this loading level, the lateral load carrying capacity of specimen started to fall off. After concrete cover of the specimen completely spalled off, the longitudinal bars and hoops outcropped and then the longitudinal bars buckled during the following cycles when the lateral displacement reaches 27.5 mm, as shown in Figure 4(f), and the fracture of the longitudinal bars was observed at subsequent larger lateral displacement which is 32.5 mm, as shown in Figure 4(g). The test continued until the global instability appeared when the lateral displacement reaches 42.5 mm. After the test, the concrete was removed and the fracture of encased steel was observed, as shown in Figure 4(h), and no encased steel buckling was found.

The typical damage development was roughly the same for the seven specimens. All specimens exhibited flexure-yielding behavior since steel web yielding occurred later than steel flange yielding, and no hoop rebar of specimens was found yielding before longitudinal rebar buckling or fracture. The typical damage development was as follows: horizontal cracking on the tensile side of the specimen, tensile yielding of the steel plate and rebar, principle tensile yielding of steel web, concrete crushing and spalling on the compressive side of the specimen, and rebar buckling and fracture.

The crack distribution of specimens Beam 1, Beam 2, and Beam 3 with different aspect ratios before concrete spalling is shown in Figure 5. With the increase of aspect ratio, the cracking region is enlarged, and more flexural cracks and less diagonal cracks occurred. The flange-web area ratio and steel ratio have little influence on the crack distribution.

3.2. Force and Deformation Characteristics. Lateral load versus chord rotation (lateral displacement divided by specimen length) hysteretic curves of specimens and corresponding skeleton curves with typical damage states marked on it are shown in Figure 6. The hysteretic curves of specimens show SRC coupling beams exhibited little pinching effect and small degradation behavior until the longitudinal rebars were fractured, which shows SRC coupling beams have excellent energy dissipation capability. By comparing specimens Beam1, Beam2, and Beam3, the hysteresis behavior is similar among these three specimens. In general, the specimen with higher aspect ratio results in smaller hysteresis loops since the lateral load resistance capacity is lower at same lateral chord rotation. By comparing specimens Beam1, Beam4, and Beam5, increase flange-web area ratio results in fuller (smaller pinching) and more stable (smaller strength degradation) hysteresis loops, since flange steel contributes to SRC coupling beam flexural behavior more than web steel. By comparing specimens Beam2, Beam6, and Beam7, increased steel ratio also results in fuller and more stable hysteresis loops, as larger steel ratio leads to more flange steel and more web steel.

Table 4 lists the mean values of chord rotation at the damage characteristic points in the specimens' skeleton

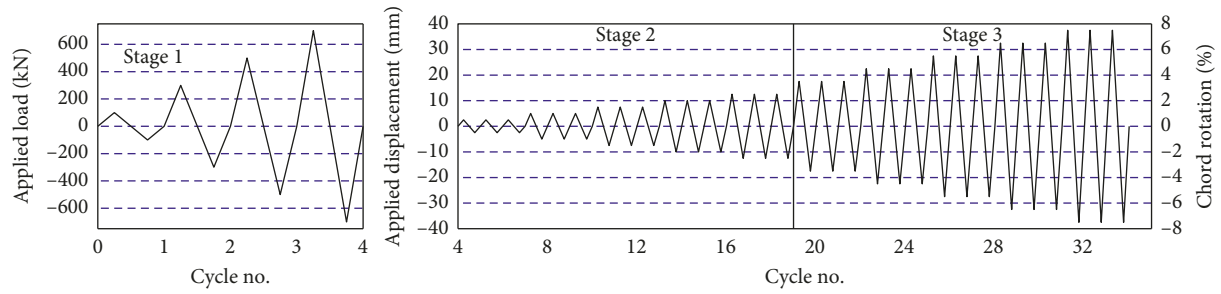


FIGURE 3: Lateral loading protocol of specimen Beam1.

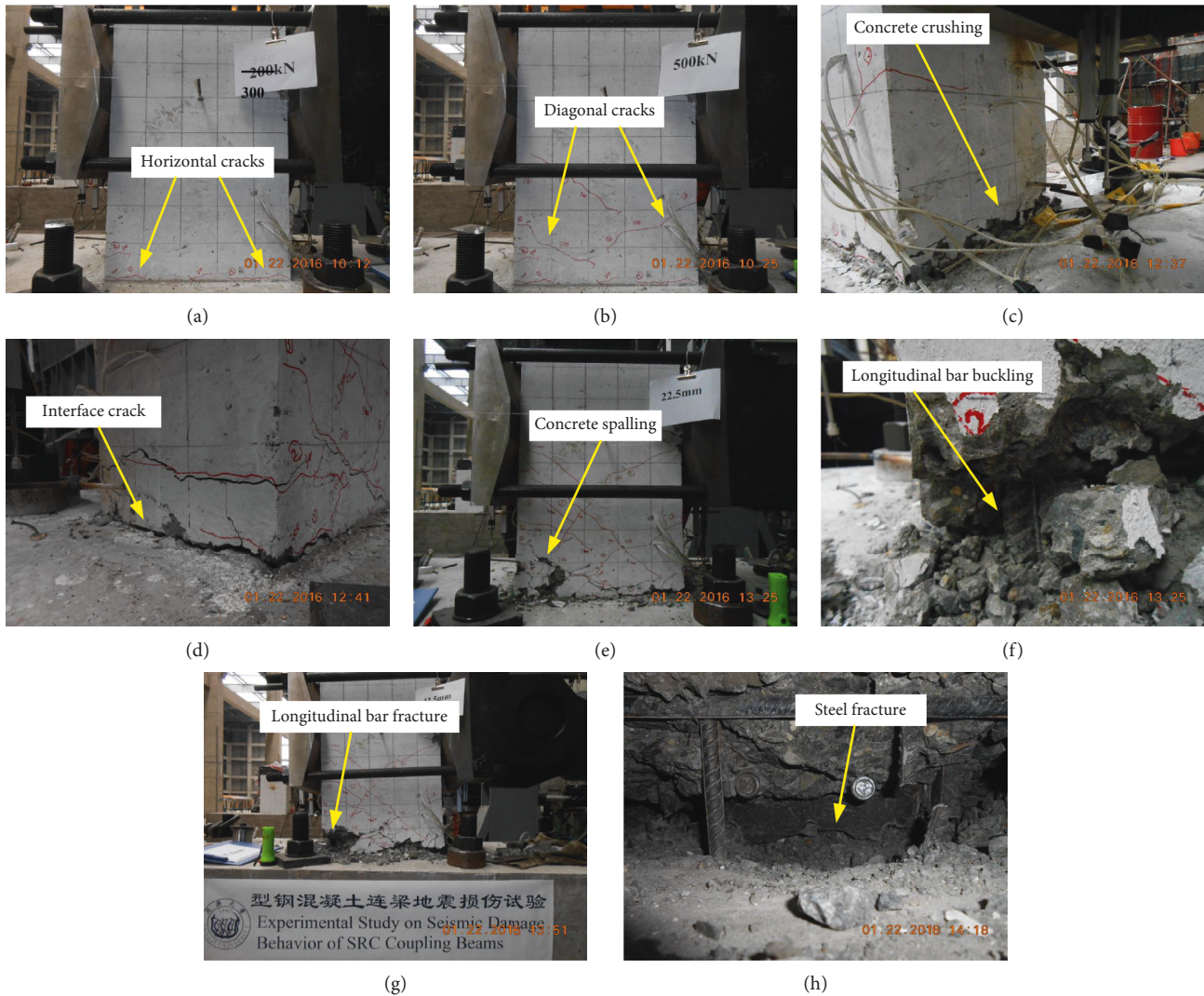


FIGURE 4: Typical damage states of specimen Beam1: (a) 300 kN (0.0012 rad), (b) 500 kN (0.003 rad), (c) 10 mm (0.02 rad), (d) 12.5 mm (0.025 rad), (e) 22.5 mm (0.045 rad), (f) 27.5 mm (0.055 rad), (g) 32.5 mm (0.065 rad), and (h) 42.5 mm (0.085 rad).

curves in two opposite loading directions. Experimental results show that although the longitudinal bars were placed outside the encased steel, encased steel still yielded before the longitudinal bars since the yielding strain of the longitudinal bars is 75% larger than the encased steel (as shown in Table 2). After the longitudinal bars fractured, the specimens can still experience larger displacement with small lateral

load carrying capacity degradation because the encased steel plate possessing much larger deformation capacity than the steel bar was still effective to resist the lateral load.

For specimens Beam1, Beam2, and Beam3 with different aspect ratios, specimen Beam1 with the aspect ratio of 2 has the largest lateral load carrying capacity, which is 1148.7 kN and is 2.46 times that of specimen Beam3 and 1.53 times that

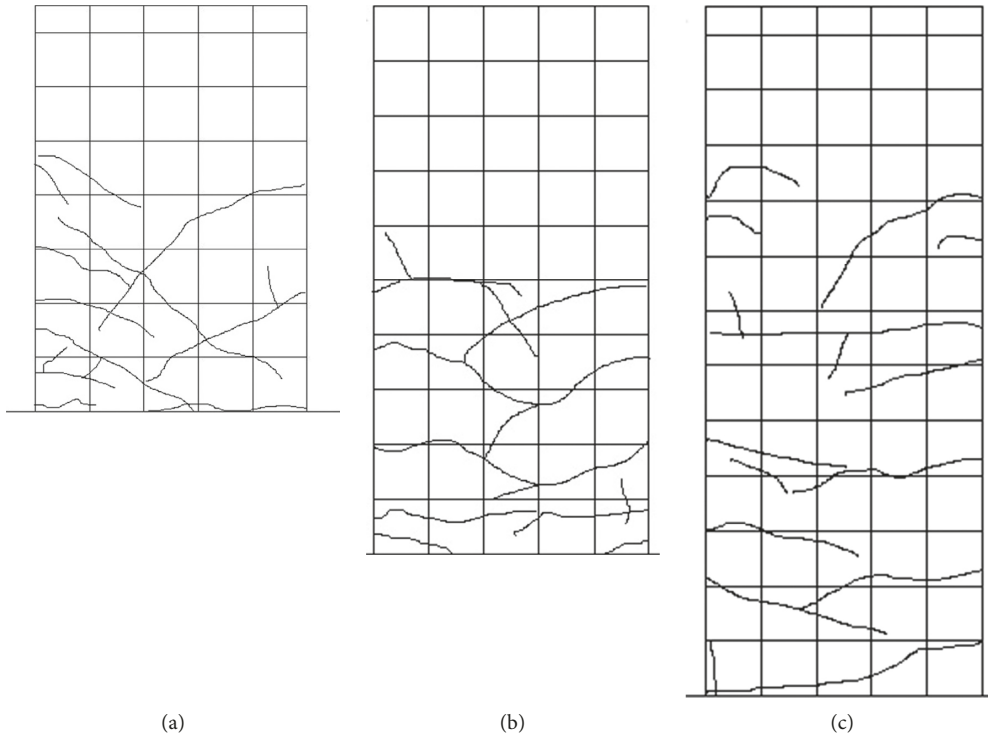


FIGURE 5: Crack pattern of specimens before concrete crushing. (a) Beam1. (b) Beam2. (c) Beam3.

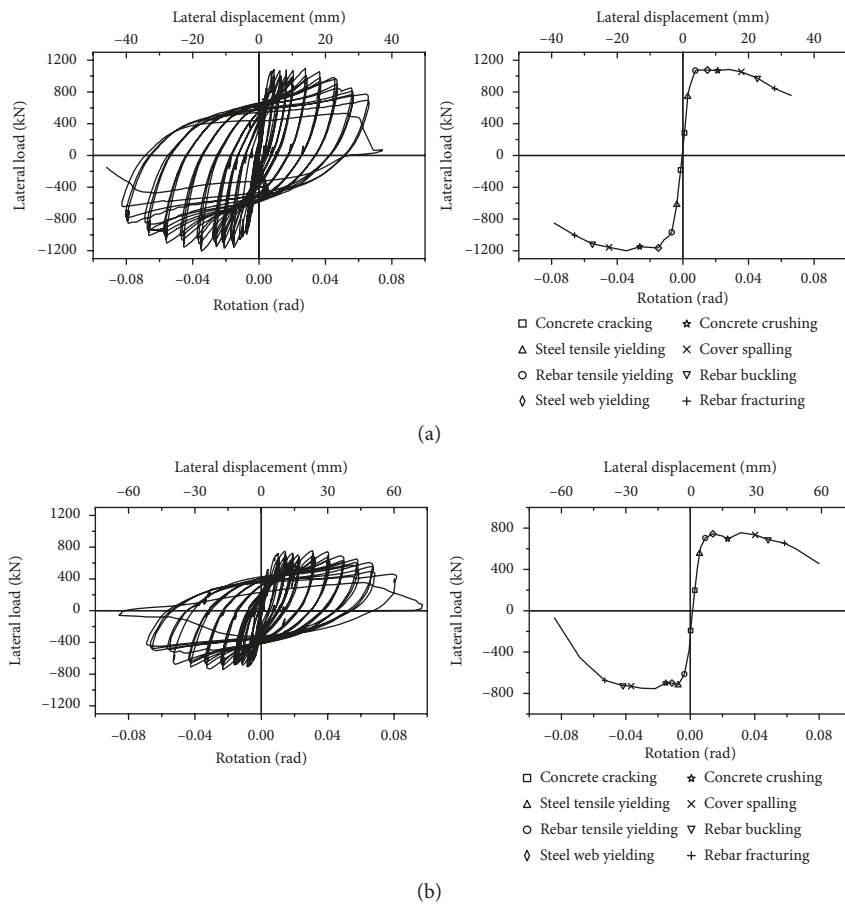


FIGURE 6: Continued.

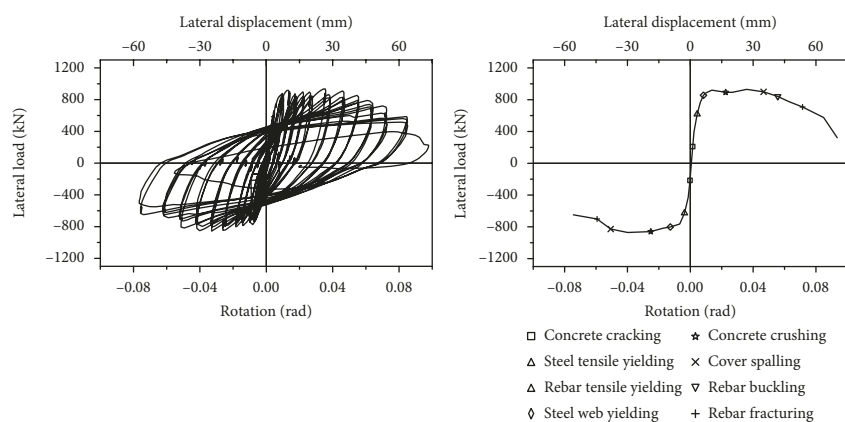
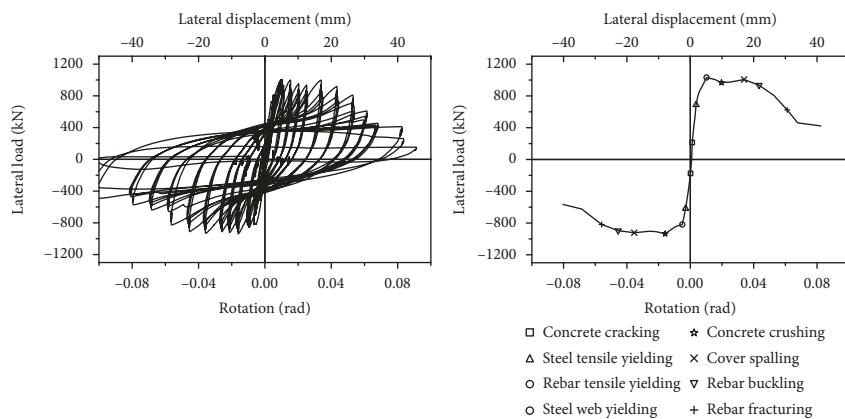
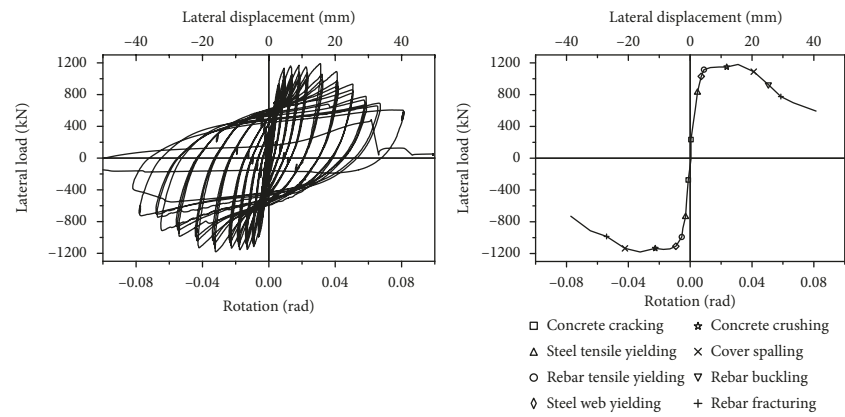
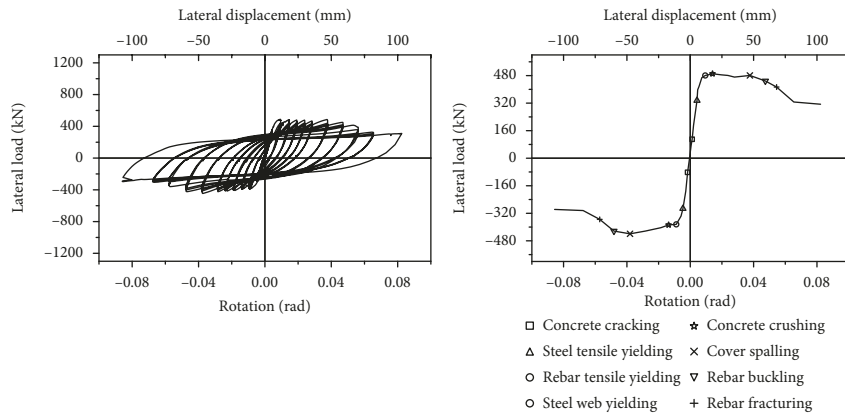


FIGURE 6: Continued.

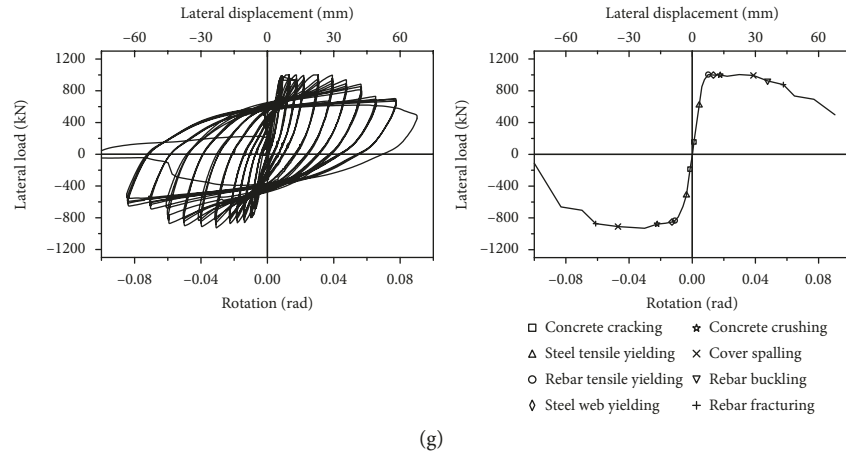


FIGURE 6: Lateral load-chord rotation hysteretic curves and skeleton curves of specimens. (a) Beam1. (b) Beam2. (c) Beam3. (d) Beam4. (e) Beam5. (f) Beam6. (g) Beam7.

TABLE 4: Chord rotation of specimens at the individual damage characteristic point.

Specimen number	θ_c (rad)	θ_{sty} (rad)	θ_{rtv} (rad)	θ_{swy} (rad)	θ_{cc} (rad)	θ_{cs} (rad)	θ_{rb} (rad)	θ_{rf} (rad)
Beam1	0.0012	0.0033	0.0072	0.0140	0.0238	0.0403	0.0502	0.0609
Beam2	0.0013	0.0063	0.0065	0.0120	0.0192	0.0385	0.0451	0.0558
Beam3	0.0014	0.0044	0.0091	0.0095	0.0139	0.0378	0.0478	0.0560
Beam4	0.0009	0.0041	0.0072	0.0085	0.0233	0.0416	0.0485	0.0565
Beam5	0.0008	0.0053	0.0078	0.0078	0.0179	0.0346	0.0444	0.0586
Beam6	0.0010	0.0065	0.0065	0.0100	0.0237	0.0485	0.0522	0.0653
Beam7	0.0013	0.0039	0.0105	0.0131	0.0201	0.0430	0.0511	0.0593

Note: θ_c , θ_{sty} , θ_{rtv} , θ_{swy} , θ_{cc} , θ_{cs} , θ_{rb} , and θ_{rf} represent the chord rotation of specimens at damage states of concrete cracking, steel tensile yielding, rebar tensile yielding, steel web principle tensile yielding, concrete crushing, concrete spalling, rebar buckling, and rebar fracture, respectively. For Beam5, rebar tensile yielding and steel web principle tensile yielding occurred at the same time. For Beam6, steel tensile yielding and rebar tensile yielding occurred at the same time.

of specimen Beam2, which means that the lateral load carrying capacity changes in inverse proportion with the aspect ratio, and all specimens reached its flexural strength. In general, the larger aspect ratio specimen tends to have smaller lateral load carrying capacity at the individual damage characteristic point. Considering displacements of the individual damage state, the initial damage states (concrete cracking, steel tensile yielding, and rebar tensile yielding) of specimen Beam3 with a aspect ratio of 5 tend to occur later than those of specimen Beam1 with a aspect ratio of 2, which is consistent with the elastic chord rotation equation of the Timoshenko cantilever beam, which is as follows:

$$\theta = \frac{\Delta}{L} = \frac{ML}{3EI} + \frac{M}{GAL}, \quad (6)$$

where M is the fixed end section moment of the cantilever beam, L is the length of the cantilever beam, E is the elastic modulus, I is the section moment inertia, G is the shear modulus, and A is the effective shear section area. When L is larger than $\sqrt{3EI/GA} \approx 0.8h$ (h is the beam section height), chord rotation θ increases with the increase of the beam length under the same fixed end moment. The damage states such as steel web principle yielding, concrete crushing, concrete spalling, rebar buckling, and rebar fracture of

specimen Beam3 tend to occur earlier than those of specimen Beam1 because specimen Beam3 has a relatively smaller moment gradient at the plastic zone, which causes flexural damages of Beam3 to occur easily, and smaller shear force in Beam3 leads to smaller shear deformation also.

For specimens Beam1, Beam4, and Beam5 with different flange-web area ratios of encased steel, specimen Beam4 with a flange-web ratio of 0.5 has the largest lateral load carrying capacity, which is 1186.6 kN and is 3.3% larger than that of specimen Beam1 and 22.5% larger than that of specimen Beam5, which means that the specimen without the flange of encased steel has a significant smaller lateral load carrying capacity. The reason that specimen Beam4 with a smaller flange-web ratio has slightly larger lateral load capacity than specimen Beam1 is that the encased steel consists of steel plates with different thicknesses and different yielding strengths, and the average yielding strength of encased steel of specimen Beam4 is slightly larger than that of specimen Beam1. The calculated lateral load capacity (M_n/L) for specimens Beam4 and Beam1 shown in Table 3 verified this explanation. Considering the displacements of individual damage states, except the damage states like steel tensile yielding and rebar tensile yielding, the other damage states of specimen Beam1 with a flange-web ratio of 1 tend to occur later than those of specimen Beam5 with a flange-web ratio

of 0. This is because the flange steel enhances the compression behavior of the concrete and delays the concrete crushing and spalling. In addition, shear deformation of specimen Beam1 with smaller web steel is larger than that of specimen Beam5 at the same damage state.

For specimens Beam2, Beam6, and Beam7, with the increase of steel ratio from 5% to 8.3%, the lateral load carrying capacity increases from 750.3 kN to 968.8 kN by 29.2%, which means that the lateral load carrying capacity of SRC coupling beam was influenced largely by the steel ratio. Except initial damage states like concrete cracking, rebar tensile yielding, and steel web principle tensile yielding, the other damage states of specimen Beam6 with a steel ratio of 6.7% tend to occur later than those of specimen Beam2 with a steel ratio of 5% and Beam7 with a steel ratio of 8.3%.

Concrete cover cracking influences the encased steel corrosion initiation and the crack width influences the corrosion propagation; thus, both influence the performance of structures [13]. The maximum residual crack width of all specimens, represented by $W_{m,ress}$, was measured during the test cycles before concrete cover crashed or spalled. The variation of maximum residual crack width with the chord rotation is shown in Figure 7. Generally, the maximum residual crack width rises up with the increase of the chord rotation. The maximum residual crack width of the specimen at the same rotation tends to be smaller with the increase of the aspect ratio or steel ratio for the average value of that for both directions. For specimens Beam1, Beam4, and Beam5 with different flange-web area ratios of encased steel, Beam4 has the smallest maximum residual crack width while Beam1 has the largest maximum residual crack width at the same rotation.

4. Numerical Analysis and Verification

4.1. Modeling. Three-dimensional nonlinear finite element models were developed to simulate the inelastic behavior of tested SRC coupling beam specimens using Abaqus [14]. Not only the global force-rotation behavior but also the local material damage behavior during the test process including concrete (cracking, crushing, and spalling), steel yielding, and rebar (yielding, buckling, and fracture) was predicted through finite element analysis. It has been reported [15–17] that material damage states, i.e., spalling and yielding, are not dependent on the history of loading but are rather closely related to the maximum displacement that the structure has experienced. Therefore, a monotonic analysis was sufficient for predicting damage deformation of flexure-yielding SRC coupling beams.

Damaged plasticity model was used to simulate the concrete inelastic behavior in SRC coupling beam specimens. This model is applicable in the situation that the concrete is at low confinement pressures (less than four to five times the largest compressive stress that can be carried by the concrete in uniaxial compression), which is suitable for SRC coupling beams. Moon et al. [18] used this model to study the confinement effect of steel tubes on the infilled concrete, and Babazadeh et al. [17] used this model to study the spalling of the concrete for RC bridge columns. The uniaxial stress-strain

relationship for the concrete recommended in Chinese code GB50010-2010 [19] was adopted here, as shown in Figure 8(a). The compression strength of the concrete is 37.3 MPa, which is the prismatic compression strength of concrete f_{ck} , which is calculated based on the conversion formula in Chinese code 50010-2010 [19], and the tested cubic compression strength of concrete f_{cu} is equal to 57.8 MPa.

Ductile damage plasticity model was used to simulate the encased steel and rebar inelastic behavior in SRC coupling beam specimens. This model offers a general capability for predicting the onset of failure and a capability for modeling progressive damage and failure of ductile metals. Zhu et al. [20] used this model to simulate the steel tearing of concrete-filled steel tube columns. The strengthening stage of steel adopted a bilinear model, hardening stiffness of which is 1% of elastic stiffness, and damage initiated at tensile strain and damage evolution adopted a linear damage form. Considering the cyclic fatigue of longitudinal rebar under earthquakes, Priestley [21] suggested the tensile strain of the longitudinal rebar to be reduced by 40%. Shi et al. [22] carried out the structural steel low cycle fatigue test and proved that the tensile strain of Q345B steel was reduced by 20.3% and Q235B steel was reduced by 38.6% after cyclic loading. The fracture strain was conservatively taken as two times tensile strain refer to the former test results. The uniaxial stress-strain relationship for the 12 mm diameter rebar is shown in Figure 8(b).

Eight-node solid elements with reduced integration (C3D8R) were used for the concrete, four-node shell elements with reduced integration (S4R) were used for the encased steel, and two-node linear displacement truss elements were used for rebar. A perfect bond was assumed between the steel, rebar elements, and the concrete part; therefore, the truss elements and shell elements were embedded in the concrete instance using the *EMBEDDED ELEMENT option. The bottom surface of the pedestal was fixed against all degrees of freedom. A reference point was modeled on the surface of the loading plate, which was constrained with the surface of the loading plate using the *COUPLING option available in the ABAQUS library.

4.2. Analysis Results. The global skeleton curves of all the specimens obtained from the FEA are compared with the skeleton curves obtained from the test, and two of them are shown in Figure 9. The FEA model gave a stiffer result in the positive part and softer one in the negative part for specimen Beam1 compared to the experimental result, which may be due to the slippage of the pedestal or the gap between loading head and specimen in the test. The local material damages obtained from FEA are also compared with test results, and concrete spalling and rebar fracture are shown in Figure 10. From the qualitative comparison, good agreement is achieved between experimental and FEA results not only on the global behavior but also on the local material damage behavior.

Concrete crushing and spalling were predicted through the compression strain of concrete. Priestley [21] suggested a value of 0.004 for cover concrete edge compressive crushing

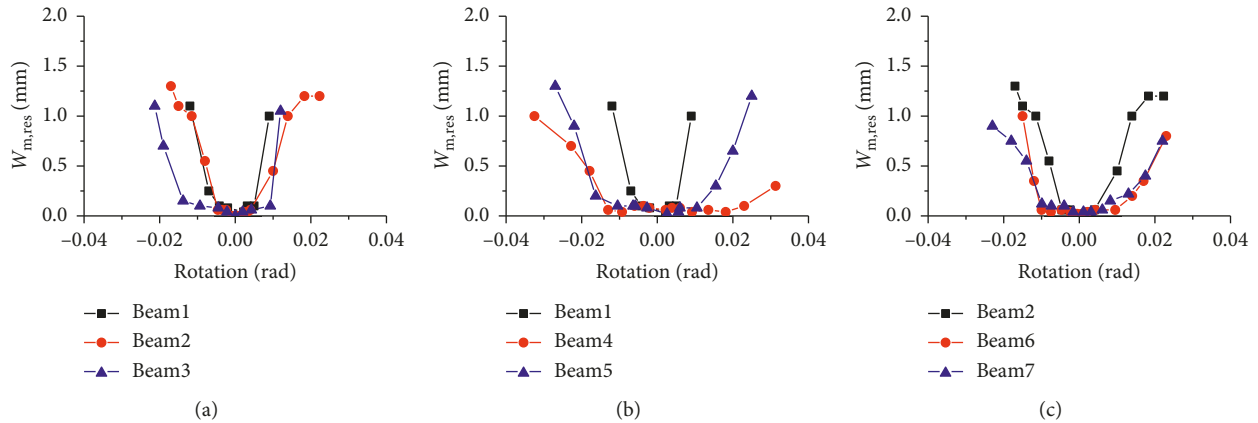


FIGURE 7: Maximum residual crack width of specimens. (a) Effect of aspect ratio. (b) Effect of flange-web ratio. (c) Effect of steel ratio.

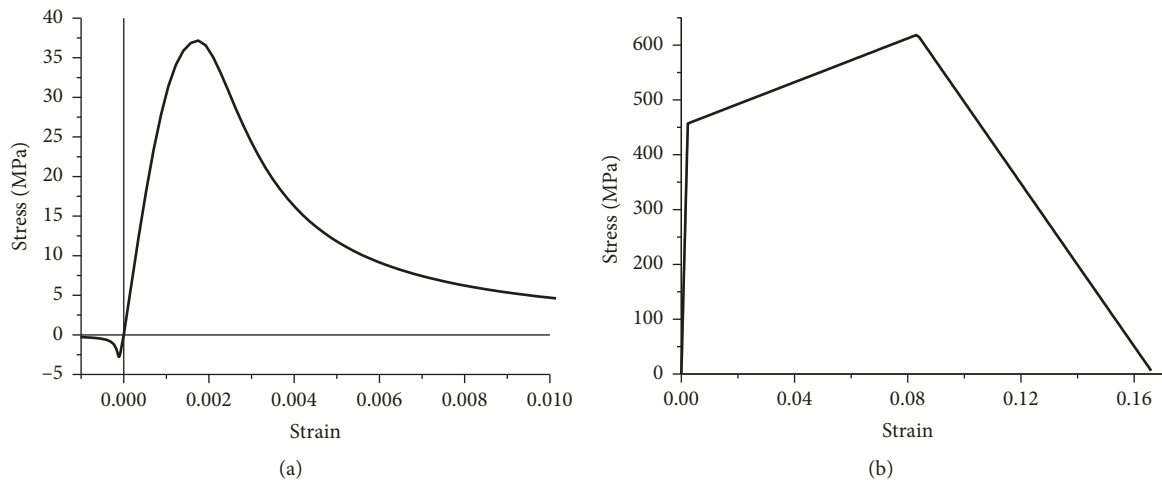


FIGURE 8: Uniaxial constitutive relationships of materials. (a) Concrete. (b) Rebar 12 mm.

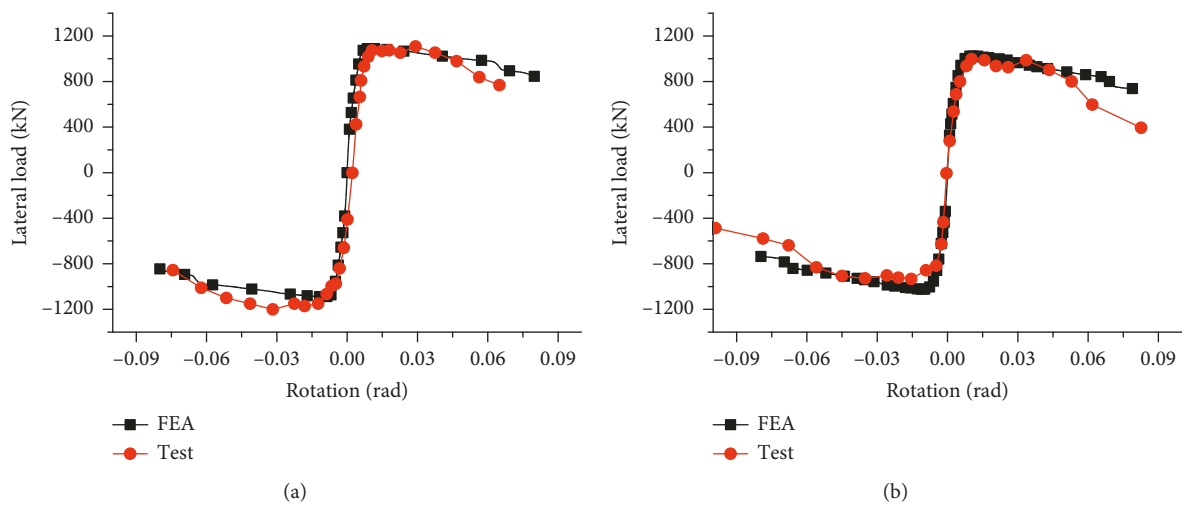


FIGURE 9: Comparison of experimental and numerical skeleton curves. (a) Specimen Beam1. (b) Specimen Beam5.

strain, and Jiang et al. [23] proposed an equation to calculate the confined concrete edge compression spalling strain, which is equal to 0.005 for test specimens. The concrete crack

width was predicted through the tensile strain of rebar. Priestley [21] suggested a value of 0.01 for longitudinal rebar tensile strain to control the residual crack width within

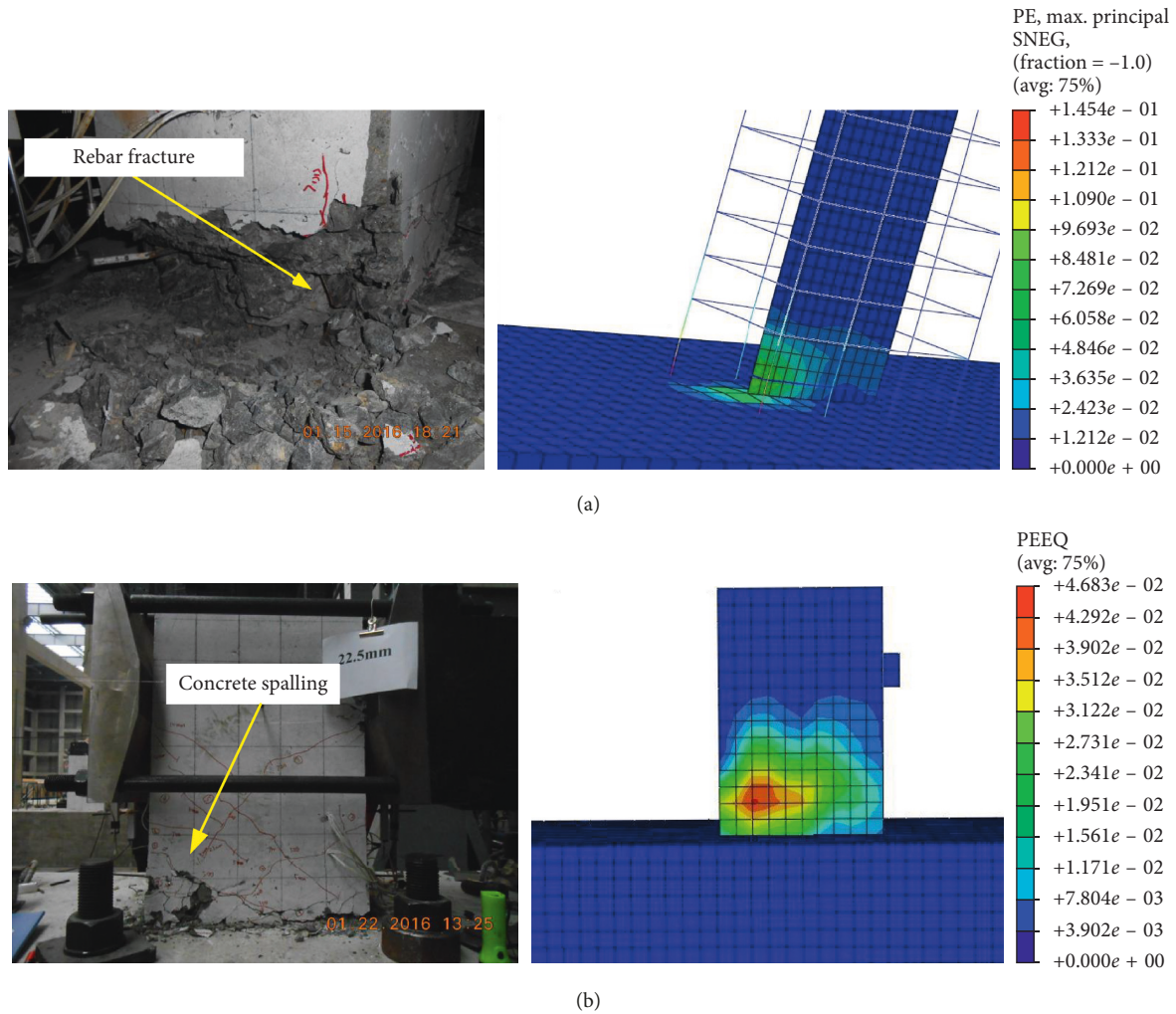


FIGURE 10: Comparison of experimental and numerical damages. (a) Rebar fracture of specimen Beam1. (b) Concrete spalling of specimen Beam1.

TABLE 5: Comparison of chord rotations of specimens for different concrete damage states.

Specimen number	Residual crack width <1 mm			Concrete crushing			Concrete spalling		
	Test	FEA	FEA/test	Test	FEA	FEA/test	Test	FEA	FEA/test
Beam1	0.0084	0.0157	1.87	0.0238	0.0231	0.97	0.0403	0.0442	1.10
Beam2	0.0116	0.0141	1.22	0.0192	0.0137	0.71	0.0385	0.0244	0.63
Beam3	0.0150	0.0155	1.03	0.0139	0.0143	1.03	0.0378	0.0256	0.68
Beam4	0.0261	0.0145	0.56	0.0233	0.0185	0.79	0.0416	0.0288	0.69
Beam5	0.0200	0.0149	0.75	0.0179	0.0196	1.09	0.0346	0.0363	1.05
Beam6	0.0187	0.0140	0.75	0.0237	0.0133	0.56	0.0485	0.0233	0.48
Beam7	0.0190	0.0141	0.74	0.0201	0.0130	0.65	0.0430	0.0225	0.52

1.0 mm. The chord rotations corresponding to different concrete damage states obtained from finite element analysis were compared with the test result, as shown in Table 5. From the quantitative comparison for concrete damage deformation, finite element analysis can only provide a statistically consistent simulation result not specifically accurate simulation result for each specimen. The mean rotation ratios between FEA and the test for the concrete residual crack width equal to 1 mm, concrete crushing, and

concrete spalling are 0.99, 0.83, and 0.74, respectively. If the cover concrete edge compression crushing strain is revised to 0.005 and confined concrete edge compression spalling strain is revised to 0.0075, the mean rotation ratios between FEA and the test for concrete crushing and concrete spalling are 1.04 and 1.03, respectively.

Steel flange tensile yielding and web principle tensile yielding were predicted directly through steel yielding strain recorded in Table 2. The chord rotations corresponding to

TABLE 6: Comparison of chord rotations of specimens for different steel damage states.

Specimen number	Steel flange yielding			Steel web yielding		
	Test	FEA	FEA/test	Test	FEA	FEA/test
Beam1	0.0033	0.0059	1.79	0.0140	0.0124	0.89
Beam2	0.0063	0.0053	0.84	0.0120	0.0116	0.97
Beam3	0.0044	0.0061	1.39	0.0095	0.0108	1.14
Beam4	0.0041	0.0051	1.24	0.0085	0.0105	1.24
Beam5	0.0053	0.0056	1.06	0.0078	0.0098	1.26
Beam6	0.0065	0.0057	0.88	0.0100	0.0115	1.15
Beam7	0.0039	0.0056	1.44	0.0131	0.0120	0.92

TABLE 7: Comparison of chord rotations of specimens for different rebar damage states.

Specimen number	Rebar yielding			Rebar buckling			Rebar fracture		
	Test	FEA	FEA/test	Test	FEA	FEA/test	Test	FEA	FEA/test
Beam1	0.0072	0.0059	0.82	0.0502	0.0777	1.55	0.0609	0.0562	0.92
Beam2	0.0065	0.0054	0.83	0.0451	0.0426	0.94	0.0558	0.0502	0.90
Beam3	0.0091	0.0060	0.66	0.0478	0.0446	0.93	0.0560	0.0571	1.02
Beam4	0.0072	0.0056	0.78	0.0485	0.0527	1.09	0.0565	0.0504	0.89
Beam5	0.0078	0.0054	0.69	0.0444	0.0526	1.18	0.0586	0.0596	1.02
Beam6	0.0065	0.0056	0.86	0.0522	0.0403	0.77	0.0653	0.0490	0.75
Beam7	0.0105	0.0057	0.54	0.0511	0.0390	0.76	0.0593	0.0493	0.83

different steel yielding states obtained from finite element analysis were compared with the test result, as shown in Table 6. The finite element analysis can provide a statistically consistent simulation result, and the mean rotation ratios between FEA and the test for steel flange tensile yielding and steel web principle tensile yielding are 1.23 and 1.08, respectively.

Rebar tensile yielding and rebar fracture were predicted directly through rebar yielding strain and tensile strain recorded in Table 2. Rebar buckling was predicted through confined concrete ultimate compressive strain, which is calculated using equation suggested by Priestley [21]. The chord rotations corresponding to different rebar damage states obtained from finite element analysis were compared with the test result, as shown in Table 7. The finite element analysis can provide a statistically consistent simulation result, and the mean rotation ratios between FEA and the test for rebar tensile yielding, rebar buckling, and rebar fracture are 0.74, 1.03, and 0.90, respectively.

4.3. Performance Index Limit Analysis. The seismic performance of SRC coupling beams is affected by the material damage, which is related to the material strain. On the other hand, the degradation of the load carrying capacity of SRC coupling beams affects its seismic performance also. Based on the study on the material damage strain limits [21, 23] and component strength degradation limits [24], four performance levels are defined, as shown in Table 8. Since there is a lack of test records of specimens' deformation at damage states of concrete strain equal to 0.002 or crack width equal to 2 mm, the chord rotation of specimens at different performance levels can only be obtained through FEA. Table 9 shows the chord

rotations of SRC coupling beam specimens at different performance levels, and then the mean values were adopted as the performance index limits, which were 0.005 rad, 0.014 rad, 0.024 rad, and 0.047 rad for the four performance levels.

5. Summary and Conclusions

Seven half-scale flexural-yielding SRC coupling beam specimens designed according to Chinese approach were tested under cyclic load. The influence of design parameters such as aspect ratio, flange-web area ratio of encased steel, and steel ratio on damage development, hysteretic behavior, strength, and maximum residual crack width were discussed. Finite element analysis was conducted for specimens; both global skeleton curves and local material damage were simulated simultaneously. Through quantitative comparison, finite element analysis can provide a statistically consistent simulation result for material damages for each specimen. Some conclusions are drawn from this research:

- (1) All specimens failed in flexural mode. The damage development was roughly the same, and the typical damage states were recorded through the whole loading process, which can be used in assessing the seismic performance level of SRC coupling beams.
- (2) With the increase of aspect ratio, the lateral load carrying capacity drops down significantly and the maximum residual crack width tends to be smaller. With the increase of flange-web area ratio of encased steel, the hysteretic curve gets fuller. The specimen with intermediate flange-web area ratio has the largest lateral load carrying capacity but smallest maximum residual crack width. With the increase of

TABLE 8: Method of defining performance levels for SRC coupling beams.

Performance level	Damage description	Performance criterion		
		Rebar or steel strain	Concrete strain	Load carrying capacity
Being basically intact	There are fine cracks in concrete, while steel or rebar is not yielding	ϵ_y	0.002	—
Slight damage	Concrete cover is not crushing, and residual crack width is less than 1 mm	0.015	0.005	—
Moderate damage	Concrete cover is not spalling, and residual crack width is less than 2 mm	0.03	0.0075	95% P_{\max}
Severe damage	Concrete core is not crushing, and rebar or steel is not fracturing	ϵ_{su}	ϵ_{cu}	85% P_{\max}

Note: ϵ_y is the yielding strain of steel or rebar, ϵ_{su} is the tensile strain of steel or rebar, ϵ_{cu} is the ultimate strain of the concrete, P_{\max} is the lateral load carrying capacity of specimens.

TABLE 9: Chord rotations of SRC coupling beams at different performance levels (rad).

Specimen number	Performance level			
	Being basically intact	Slight damage	Moderate damage	Severe damage
Beam1	0.0055	0.0157	0.0264	0.0562
Beam2	0.0053	0.0137	0.0212	0.0426
Beam3	0.0060	0.0143	0.0235	0.0446
Beam4	0.0051	0.0145	0.0239	0.0504
Beam5	0.0054	0.0149	0.0257	0.0526
Beam6	0.0051	0.0133	0.0228	0.0403
Beam7	0.0050	0.0130	0.0228	0.0390

steel ratio, the lateral load carrying capacity increases significantly while the maximum residual crack width drops down.

- (3) The finite element model was benchmarked through comparison with test results for both global load-deformation curves and local material damages. Both qualitative and quantitative comparisons testify the accuracy of finite element models. The cover concrete edge compression strain and confined concrete edge compression strain were recommended to be 0.005 and 0.0075, respectively, for accurately modeling concrete crushing and spalling. Based on the damage characters and strength degradation, four performance levels were defined and corresponding chord rotation limits were obtained through the verified numerical analysis.

Data Availability

All the data in this paper are obtained from tests and numerical analysis, and no other data in the literature are used to support this study.

Conflicts of Interest

The authors declare that there are no potential conflicts of interest with respect to the research, authorship, and publication of this article.

Acknowledgments

The financial support from the Program of Shanghai Academic Research Leader (grant number 18XD1403900) and the National Key Research and Development Program of China (grant number 2017YFC1500701) is gratefully acknowledged.

References

- [1] S. El-Tawil, K. A. Harries, P. J. Fortney, B. M. Shahrooz, and Y. Kurama, "Seismic design of hybrid coupled wall systems: state of the art," *Journal of structural engineering*, vol. 136, no. 7, pp. 755–769, 2010.
- [2] C.-C. Hung and W.-T. Lu, "A performance-based design method for coupled wall structures," *Journal of Earthquake Engineering*, vol. 21, no. 4, pp. 579–603, 2016.
- [3] C. J. Motter, D. C. Fields, J. D. Hooper et al., "Steel-reinforced concrete coupling beams. I: testing," *Journal of Structural Engineering*, vol. 143, no. 3, article 04016191, 2016.
- [4] B. Gong and B. M. Shahrooz, "Concrete-steel composite coupling beams. I: component testing," *Journal of Structural Engineering*, vol. 127, no. 6, pp. 625–631, 2001.
- [5] B. Gong and B. M. Shahrooz, "Concrete-steel composite coupling beams. II: subassembly testing and design verification," *Journal of Structural Engineering*, vol. 127, no. 6, pp. 632–638, 2001.
- [6] R. K. L. Su and W. Y. Lam, "A unified design approach for plate-reinforced composite coupling beams," *Journal of Constructional Steel Research*, vol. 65, no. 3, pp. 675–686, 2009.

- [7] C. J. Motter, D. C. Fields, J. D. Hooper et al., "Steel-reinforced concrete coupling beams. II: Modeling," *Journal of Structural Engineering*, vol. 143, no. 3, article 04016192, 2016.
- [8] Q. Z. Liang and X. L. Han, "The behavior of stiffening beams and lintel beams under cyclic loading," *Journal of South China University of Technology*, vol. 23, no. 1, pp. 27–33, 1995, in Chinese.
- [9] H. Jiang, B. Wang, and X. Lu, "Experimental study on damage behavior of reinforced concrete shear walls subjected to cyclic loads," *Journal of Earthquake Engineering*, vol. 17, no. 7, pp. 958–971, 2013.
- [10] J. Yue, J. Qian, and D. E. Beskos, "A generalized multi-level seismic damage model for RC framed structures," *Soil Dynamics and Earthquake Engineering*, vol. 80, pp. 25–39, 2016.
- [11] JGJ138-2016, *Code for Design of Composite Structures*, China Architecture & Building Press, Beijing, China, 2016.
- [12] R. D. Lequesne, G. J. Parra-Montesinos, and J. K. Wight, "Seismic behavior and detailing of high-performance fiber-reinforced concrete coupling beams and coupled wall systems," *Journal of Structural Engineering*, vol. 139, no. 8, pp. 1362–1370, 2012.
- [13] M. Otieno, H. Beushausen, and M. Alexander, "Towards incorporating the influence of cover cracking on steel corrosion in RC design codes: the concept of performance-based crack width limits," *Materials and Structures*, vol. 45, no. 12, pp. 1805–1816, 2012.
- [14] SIMULIA, *Dassault Systems. ABAQUS Analysis User's Manual, Version 6.16*, SIMULIA, Johnston, RI, USA, 2016.
- [15] J. C. Goodnight, M. J. Kowalsky, and J. M. Nau, "Effect of load history on performance limit states of circular bridge columns," *Journal of Bridge Engineering*, vol. 18, no. 12, pp. 1383–1396, 2013.
- [16] R. T. Ranf, "Damage accumulation in lightly confined reinforced concrete bridge columns," PEER Report, Pacific Earthquake Engineering Research Center, University of California, Berkeley, CA, USA, 2006.
- [17] A. Babazadeh, R. Burgueño, and P. F. Silva, "Use of 3D finite-element models for predicting intermediate damage limit states in RC bridge columns," *Journal of Structural Engineering*, vol. 141, no. 10, article 04015012, 2015.
- [18] J. Moon, C. W. Roeder, and H.-E. Lee, "Analytical modeling of bending of circular concrete-filled steel tubes," *Engineering Structures*, vol. 42, no. 12, pp. 349–361, 2012.
- [19] GB50010-2010, *Code for Design of Concrete Structures*, China Architecture & Building Press, Beijing, China, 2010.
- [20] H. Zhu, M. T. Stephens, and D. E. Lehman, "Inelastic response prediction of CFST columns and connections subjected to lateral loading," *Journal of Constructional Steel Research*, vol. 132, pp. 130–140, 2017.
- [21] M. J. N. Priestley, "Performance based seismic design," in *Proceedings of 12th World Conference on Earthquake Engineering*, Auckland, New Zealand, January 2000.
- [22] Y. Shi, M. Wang, and Y. Wang, "Experimental and constitutive model study of structural steel under cyclic loading," *Journal of Constructional Steel Research*, vol. 67, no. 8, pp. 1185–1197, 2011.
- [23] H. Jiang, X. Lu, and T. Kubo, "Damage displacement estimation of flexure-dominant RC columns," *Advances in Structural Engineering*, vol. 13, no. 2, pp. 357–368, 2010.
- [24] GB50011-2010, *Code for Seismic Design of Buildings*, China Architecture & Building Press, Beijing, China, 2010.

